Journal of Alloys and Compounds 509 (2011) 8832–8839

Contents lists available at ScienceDirect

Journal of Alloys and Compounds

journal homepage: www.elsevier.com/locate/jallcom

# Microstructures and mechanical properties of Mg–10Gd–6Y–2Zn–0.6Zr(wt.%) alloy

Liang Zheng, Chuming Liu*, Yingchun Wan, Pingwang Yang, Xin Shu

*School of Materials Science and Engineering, Central South University,Changsha 410083, China*

ARTICLE INFO

*Article history:*
Received 23 April 2011
Received in revised form 19 June 2011
Accepted 21 June 2011
Available online 28 June 2011

*Keywords:*
Microstructures
Mechanical properties
Mg–10–Gd–6Y–2Zn–0.6Zr alloy
Strengthening models
LPSO structure

ABSTRACT

Microstructures and tensile mechanical properties of Mg–10Gd–6Y–2Zn–0.6Zr alloy were systematically studied. Four phases were found in the as-cast specimen: α-Mg, $Mg_3$(GdYZn), $Mg_{12}$(GdY)Zn and $Mg_{24}$(GdYZn)$_5$. The long-period stacking order (LPSO) structure is found, which is the phase of $Mg_{12}$(GdY)Zn. The LPSO structure has two existing forms: lamellar structure in the inner grains and block-like structure at grain boundaries. 6H-type LPSO structure with a stacking sequence of ABCBCB′ is defined in homogenized specimen, where A and B′ layers are significantly enriched by Gd, Y and Zn. The ageing hardening behavior of as-extruded specimens at 200 °C has been investigated. The ultimate tensile strengths of the as-extruded and peak-aged alloys are 360 MPa and 432 MPa, and the elongations are 18% and 5% respectively. The effective strengthening models have been considered to predict the strength. The results suggested that the sub-micron metastable β′ phase was the main strengthening factor of the peak-aged alloy.



## 1. Introduction

Magnesium alloys with rare earth (RE) metals have received a tremendous amount of attention due to their low density and good mechanical properties, such as high strength at room and elevated temperatures [1–4]. However, the application of Mg–RE alloys has been limited due to their inferior ductility. Many researchers tried to improve the mechanical properties by developing original techniques. High yield strength, 330 MPa, is obtained by introducing friction stir processing (FSP) into Mg–10Gd–3Y–0.5Zr cast [5]. Peng et al. [6] reported that cyclic extrusion and compression (CEC) at 450 °C can refine the microstructure of GW102K Mg alloy. Precipitation strengthening is another attractive topic due to the large solid solution of Mg–RE alloys. A four-stage precipitation sequence is determined: α-Mg(S.S.S.S) → β″(DO19) → β′(bco $Mg_{15}X_3$) → $\beta_1$ → β(fcc $Mg_5$Gd) [7]. The predominant strengthening mechanism of the peak-aged Mg–RE alloys at room temperature is grain boundary strengthening and precipitation hardening [8]. High-temperature equal-channel angular pressing (ECAP) can modify precipitate microstructure to obtain precipitation strengthening [9]. Barucca et al. [10] reported that the hardening mechanism during ageing at 150 °C was based on β″ transformation of pre-precipitates and their growth, while at 210 °C hardening mechanism was mainly associated with β″ → β′ transformation.

Many investigators discovered the LPSO structure in Mg–Zn–Gd Mg–Zn–Y alloys [11–16]. The cooling rate is an important factor for the formation of 14H-LPSO structure in as-cast GWZ1032K alloy [13]. The LPSO structure has broad application prospects to improve the mechanical properties of magnesium alloys. Given the superior strength of the Mg–Gd–Y–Zn–Zr alloys, a better understanding of the microstructural constituents and precipitation process in these alloys is essential in optimizing alloy design. In this paper, the phase compositions, ageing hardening behavior, microstructure and mechanical properties of the as-extruded and peak-aged Mg–10Gd–5Y–2Zn–0.6Zr alloy have been investigated. The strengthening mechanisms of the alloy are discussed by building strengthening models to predict the theoretical yield strength.

## 2. Experimental procedures

The alloy ingots with nominal composition of Mg–10Gd–6Y–2Zn–0.4Zr (wt%) were prepared in an electric resistance furnace at about 750–780 °C under a mixed atmosphere of $CO_2$ and $SF_6$ with a volume ratio of 99:1. At about 730 °C, the melts were poured into steel mold with an ingot diameter of 65 mm. The ingots were homogenized at 520 °C for 16 h, and then quench in 80 °C water. The homogenized ingots were milled into round ingots with a diameter of 58 mm, and then extruded into rods with a diameter of 14.5 mm at 480 °C in one pass. Some of the rods were directly aged at 200 °C in an air electric resistance furnace.

Tensile tests were carried out using the universal tensile testing machine at a cross-head speed of 2 mm/min at room temperature, with the tensile axis paral-

* Corresponding author. Tel.: +86 731 8887 7502; fax: +86 731 8883 0257.
*E-mail address:* cmLiu@mail.csu.edu.cn (C. Liu).

0925-8388/$ – see front matter © 2011 Elsevier B.V. All rights reserved.
doi:10.1016/j.jallcom.2011.06.090

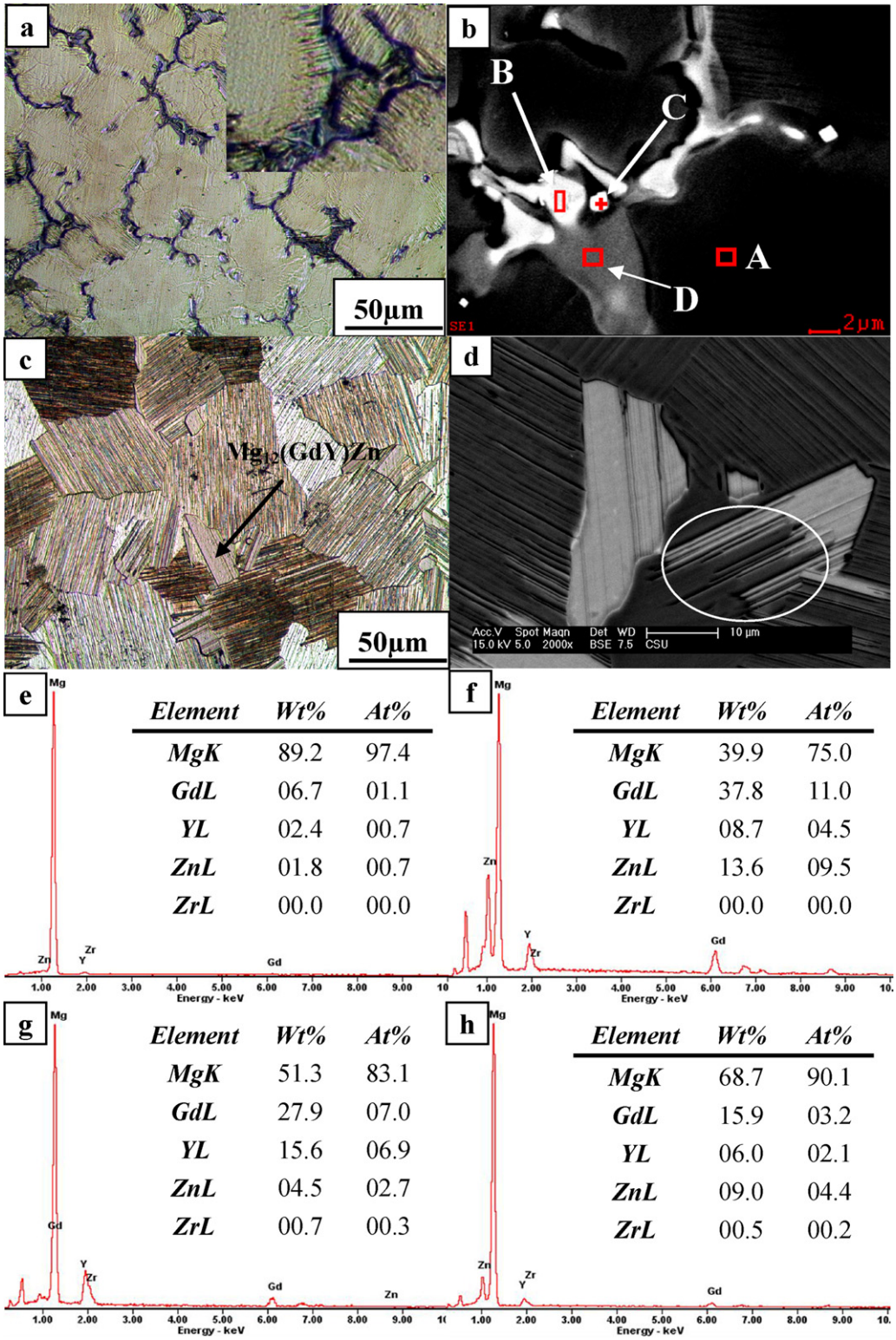


**Fig. 1.** (a) OM image of the as-cast specimen; (b) SEM image of as-cast specimen; (c) OM image of the homogenized specimen; (d) SEM image of the homogenized specimen; (e) EDS result of point A; (f) EDS result of point B; (g) EDS result of point C; (h) EDS result of point D.

leled to the extrusion direction. Vickers hardness testing was taken using 4.9 N load and holding time of 15 s. Microstructural examination was performed using a Leica optical microscope (OM) and Sirion200 field emission scanning electron microscope (SEM) at 15 kV. Samples for metallography were etched in a solution of 6 g picric acid, 40 ml acetic acid, 40 ml water and 100 ml ethanol. The grain size was determined on the photographs using lineal intercept method outlined in accordance with ASTM standard E112-96. Transmission electron microscope (TEM) and high resolution transmission electron microscope (HRTEM) observation were performed using a JEM 2100F HRTEM operated at 200 kV. Specimens for TEM were prepared with an argon ion milling technique. The constituent phases were identified by D/Max2500 X-ray diffraction (XRD) at 36 kV and GENESIS-60S energy dispersive spectroscope (EDS).

## 3. Results and discussion

### 3.1. The microstructures of the as-cast and homogenized alloys

The microstructure of the as-cast specimen is shown in Fig. 1a. It can be seen that eutectic compounds are distributed at grain boundaries, and the average grain size is about 50 μm. According to the SEM images (Fig. 1b) the as-cast alloy mainly consists of four phases: α-Mg, Network shaped phase, block shaped compounds and gray phase. According to the EDS result (Fig. 1e), Matrix of primary α-Mg solid solution (Fig. 1b point A) is supersaturated with Gd, Y and Zn. The chemical composition of the Network shaped phase (Fig. 1b point B) is Mg–11at%Gd–4.5at%Y–9.5at%Zn (Fig. 1f), this indicates the stoichiometry of network shaped phases is near $Mg_3(GdYZn)$. The chemical composition of the block shaped compounds (in Fig. 1b point C) is Mg–7at%Gd–6.9at%Y–2.7at%Zn according to the EDS result (Fig. 1g), this indicates the stoichiometry of the block shaped compounds is near $Mg_{24}(GdYZn)_5$. The gray phase around the matrix (Fig. 1b point D) is $Mg_{12}(GdY)Zn$ phase according to the EDS result(Fig. 1h). Fine-lamellar structure seen clearly in the OM image (in Fig. 1a) is tending to grow to the interior of grains. Many investigators claimed that the fine-lamellar structure was different from the $Mg_{12}(GdY)Zn$, and this kind of structure was named as the LPSO phase after the atomic arrangement [12–16]. However, except the four phases mentioned above, no specific phase can be determined by XRD (Fig. 2), and the chemical composition of the so-called LPSO structure is near $Mg_{12}(GdY)Zn$[17]. In order to identify the relationship between the LPSO structure and the $Mg_{12}(GdY)Zn$, the morphology and the composition of the $Mg_{12}(GdY)Zn$ in the homogenized specimen were investigated. The chemical composition is identical with that of the as-cast specimen. In contrast to the as-cast specimen, lamellar structures are found in the $Mg_{12}(GdY)Zn$ phase of the homogenized specimen, with the morphology very similar to that of the LPSO structure in the matrix. Moreover, the acicular $Mg_{12}(GdY)Zn$ phase in the white circle(Fig. 1d) elongates to the interior of the grain. It is easy to say that the LPSO structure and the $Mg_{12}(GdY)Zn$ are the same phase.

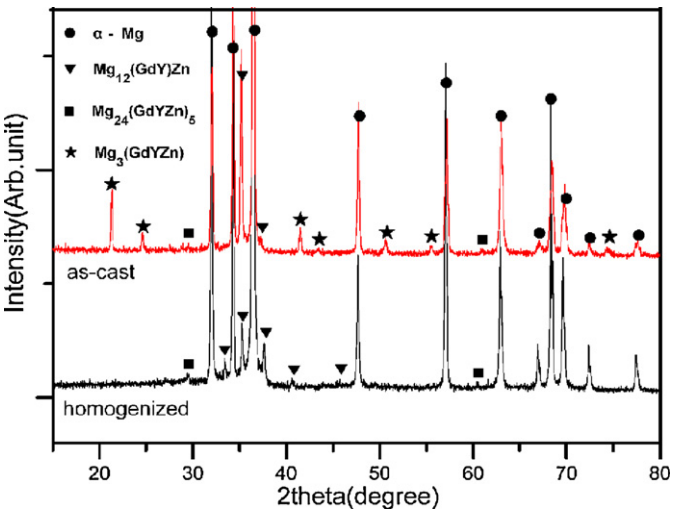


**Fig. 2.** XRD patterns of the as-cast and homogenized specimens.

In accordance with the OM and SEM images of the homogenized specimen (Fig. 1c and d), the $Mg_3(GdYZn)$ has already been solid dissolved in α-Mg, and it is confirmed by the XRD result (Fig. 2). In order to investigate the microstructure of the LPSO structure found in the alloy, the TEM observation of the $[0\,1\,\bar{1}\,0]$ zone axis has been conducted. Fig. 3a is the BF image of the LPSO structure in the as-cast alloy. The fine lamellar LPSO structures pass through the eutectic phase in the grain boundary, and grow to the grain interior. For the purpose of understanding the growth of LPSO structure, the BF TEM image of the homogenized specimen is given in Fig. 3b.

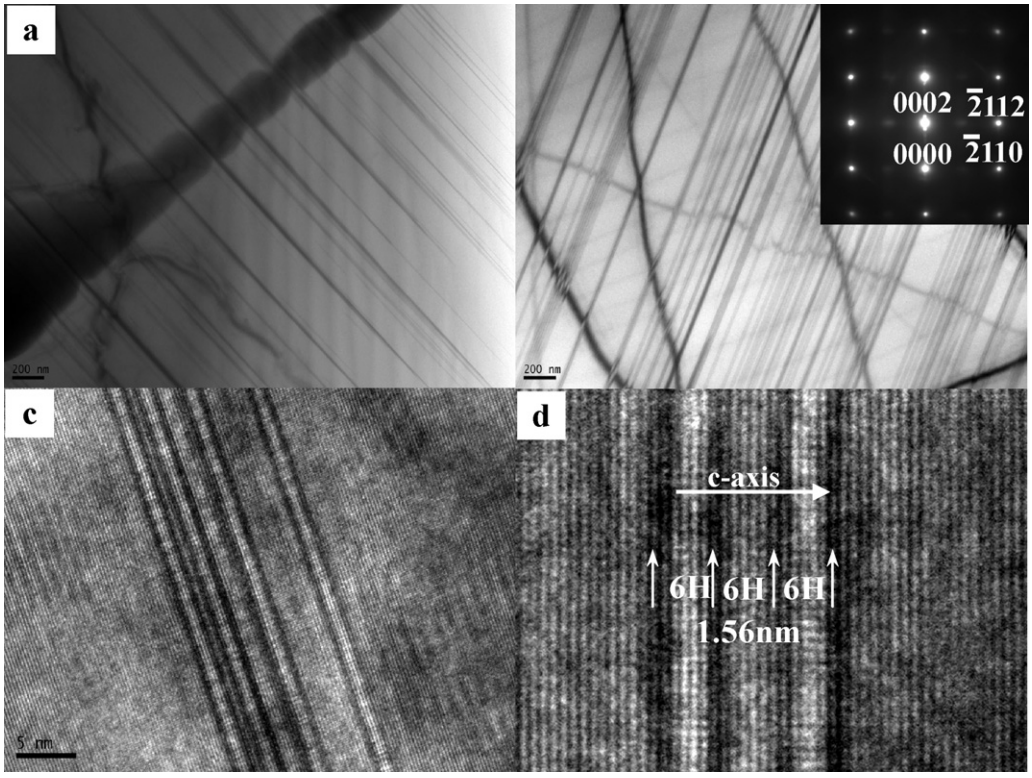


**Fig. 3.** (a) TEM BF image of the as-cast specimen; (b) TEM BF image of the homogenized specimen; (c) HRTEM image of LPSO structure ($B//[0\ 1\bar{1}0]$); (d) Magnified image of LPSO structure.

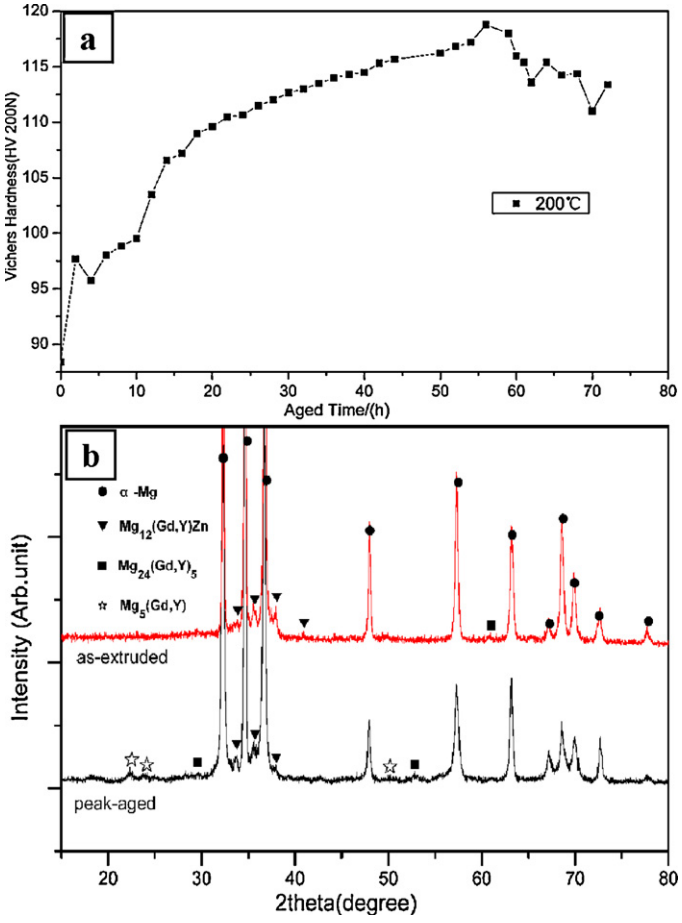


**Fig. 4.** (a) Precipitation hardening curves of GWZ1062 alloy at 200 °C (b) XRD patterns of the as-extruded and peak-aged specimens.

The LPSO structures are coarser and more intensive than that in the as-cast specimen. HRTEM image of the $[0\,1\,\bar{1}\,0]$ zone axis was taken from this structure, as shown in Fig. 3c and d. The HRTEM image shows a stacking sequence of ABCBCB′, which is perpendicular to the c-axis of the HCP Mg-matrix and suggests a 6H-type structure, where A and B′ layers are significantly enriched by RE and Zn [18]. The thickness of one 6H-type structure is 1.56 nm = 3*c*, and *c* is a lattice constant of the HCP Mg structure. During solidification, the LPSO structure nucleated at the grain boundaries and grew to the interior of grains through the diffusion of the Zn and RE atoms. However, there was not enough time for Zn and RE atoms to diffuse due to the high cooling rate (1 K/s). Instead, they concentrated at the grain boundaries mainly in the form of eutectic compounds $Mg_3(GdY)$ and $Mg_{12}(GdY)Zn$, so the growth of the LPSO structure was inhibited. Once the as-cast specimens were exposed to elevated temperature, the diffusion of Zn and RE atoms would be activated. Zn and RE atoms replaced the Mg atoms and formed LPSO structures in the form of 6H-type stacking sequence. Besides the growth along the longitudinal direction, it could also grow along the transverse direction, and becoming coarse gradually. Fig. 1c and d shows the OM and SEM images of LPSO structures in homogenized specimen, some of the LPSO structures have already penetrated into the whole grain, and showed the orientation of the matrix by its unique image.

### 3.2. Ageing hardening behavior of the as-extruded alloy

Fig. 4a shows the precipitation hardening curve of the as-extruded specimens at 200 °C. The alloy exhibits an obvious age hardening response. The hardness of the as-extruded alloy is 86 HV, and increases obviously in the first 15 h of ageing, and then the increment speed of the hardness slows down gradually. Peak hardness is obtained after 56 h, with a value of 118 HV. According to the XRD results (Fig. 4b), plenty of $Mg_5(GdY)$ precipitated after ageing for 56 h, and that is the reason of the improvement of the hardness value.

Fig. 5 shows the OM images of the as-extruded and the peak-aged specimens. It is easy to say that almost all the LPSO structures have been distorted and distributed along the extrusion direction. There are a lot of fine dynamic recrystallization (DRX) grains around the LPSO structure (Fig. 5b). The microstructure of the alloy has been remarkably refined compared with that of the homogenized alloy. The average grain sizes of the as-extruded and peak-aged alloys are about 4.7 μm.

Fig. 6 shows the SEM images and corresponding EDS results of the as-extruded specimens. The white LPSO structure can be seen clearly. The lamellar and block-like LPSO structures are both extended along the extrusion direction (Fig. 6b), and this suggests a good plasticity of the LPSO structure. The result of linear SEM-EDS in Fig. 6a suggests that the LPSO structures are enriched by Gd, Y and Zn. The composition of the LPSO structure in the as-extruded specimen is Mg–6.2at% RE–4.4at% Zn according to the EDS result of the LPSO structure (Fig. 6c), and this composition is identical to that of the as-cast and homogenized specimens.

### 3.3. Mechanical behavior

Fig. 7 gives the nominal stress–strain curves (a) and the tensile mechanical properties (b) of the as-extruded and peak-aged specimens. The ultimate tensile strength ($\sigma_{UTS}$) of the as-extruded specimen is 360 MPa and the elongation ($\delta$) reaches to 18%. It is uncommon in Mg–Gd–Y alloys. After ageing at 200 °C for 56 h, the tensile proof strength ($\sigma_{TPS}$) increases from 270 MPa to 360 MPa, and the $\sigma_{UTS}$ from 360 MPa to 432 MPa. The good plasticity of the LPSO structure should be considered as one of the reasons for the high elongation of the as-extruded specimen. In addition, the grain growth during hot extrusion is extremely inhibited by the LPSO structure distributed at the grain boundaries, and this also led to improvement of the elongation.

Fig. 8 shows the TEM images of the peak-aged specimen from different directions. Fig. 8a and b shows the BF image of the precipitation and the corresponding selected area electron diffraction (SEAD) pattern ($B//[2\,\bar{1}\,\bar{1}\,0]$) respectively, the extra diffraction spots located at $1/4(0\,1\,\bar{1}\,0)_\alpha$, $1/2(0\,1\,\bar{1}\,0)_\alpha$ and $3/4(0\,1\,\bar{1}\,0)_\alpha$. Fig. 8d and e shows the TEM BF image and corresponding SEAD pattern (B//[0 0 0 1]) respectively. The extra diffraction spots at 1/2 distance of $(1\,\bar{1}\,0\,0)_\alpha$ or $(2\,\bar{1}\,\bar{1}\,0)_\alpha$ with the ones surrounding them. Such a diffraction feature is typical in Mg–RE alloys containing a base-centered orthorhombic (bco) structure precipitation with lattice parameters $a = 2 \times a_{\alpha-Mg} = 0.64$ nm, $b = 8 \times d(1\,0\,\bar{1}\,0)_{\alpha-Mg} = 2.22$nm, $c = c_{\alpha-Mg} = 0.52$ nm [19]. The orientation relationships between the $\beta$' phase and the α-Mg matrix are $(0\,0\,1)_{\beta'}//(0\,0\,0\,1)_\alpha$ and $[1\,0\,0]_{\beta'}//[2\,\bar{1}\,\bar{1}\,0]_\alpha$. The HRTEM images of different zone axes are shown in Fig. 8c ($B//[2\,\bar{1}\,\bar{1}\,0]$) and f (B//[0 0 0 1]). The $\beta'$ phase shows a notable morphology difference of different zone axes. Fig. 8g shows that the precipitation is dispersively distributed between two lamellar LPSO structures. It is the LPSO structure that leads to the dispersive distribution of the $\beta'$ phase in the grains.

## 4. Strengthening model

In order to predict the strengthening contributions of the extruded and peak-aged alloys quantitatively, several strengthen-

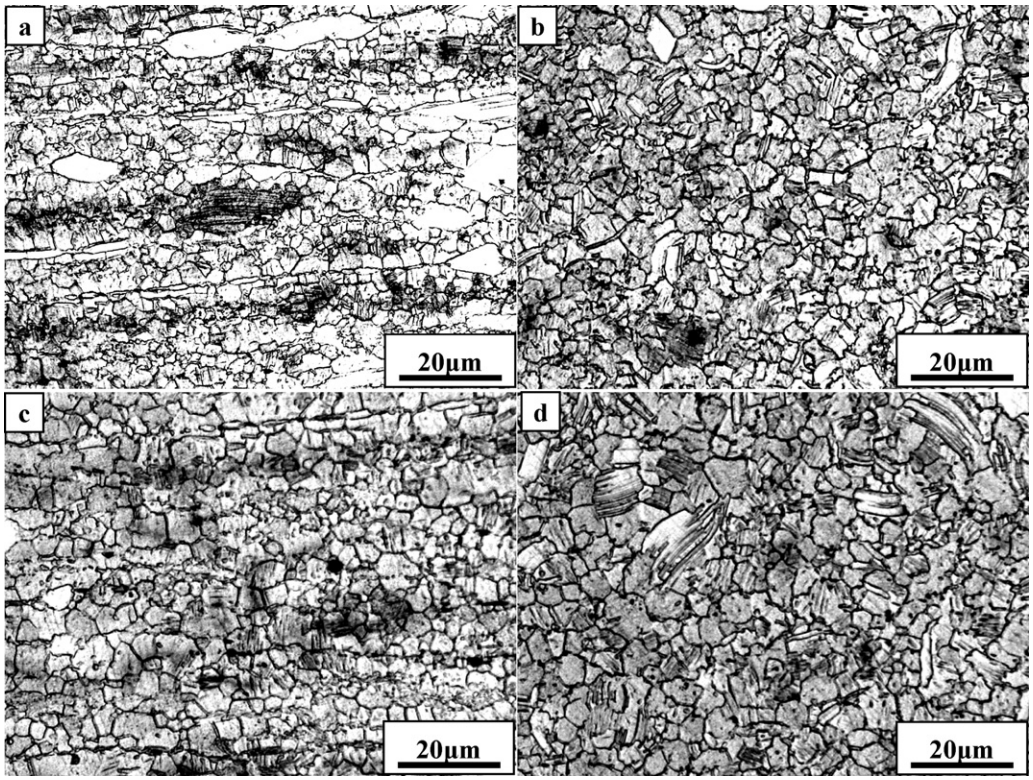


**Fig. 5.** OM images of the specimens of the as-extruded and peak-ageing; (a) Longitudinal direction image of the as-extruded specimen; (b) Transverse direction image of the as-extruded specimen; (c) Longitudinal direction image of the peak-aged specimen; (d) Transverse direction image of the peak-aged specimen.

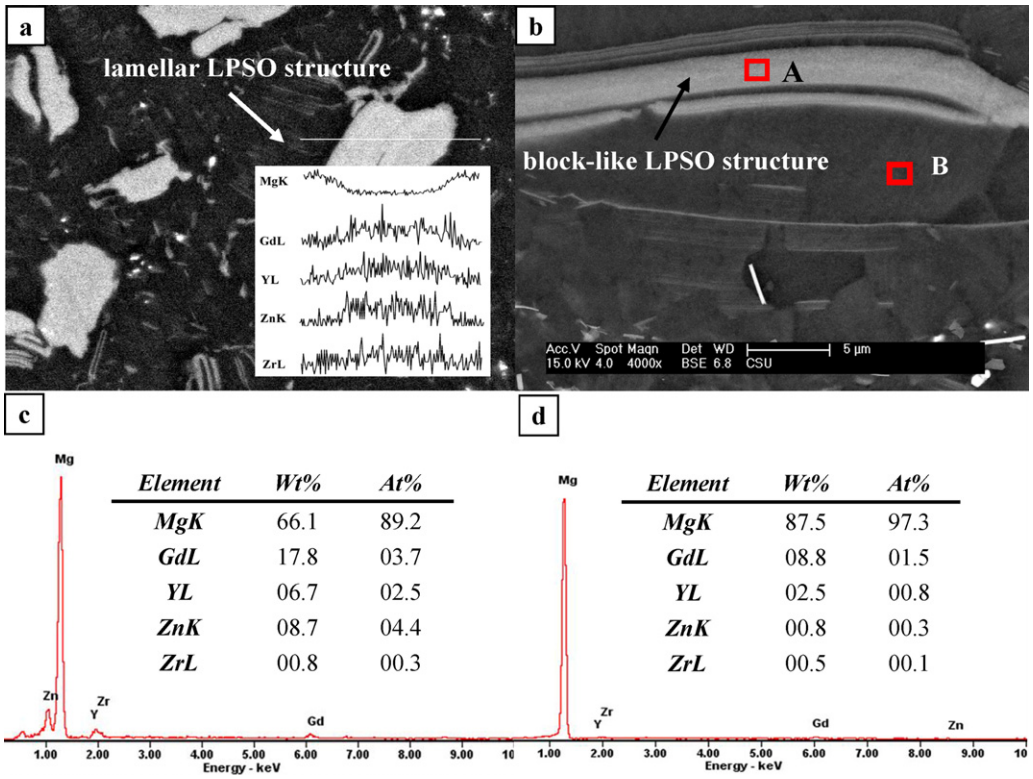


| *Element* | *Wt%* | *At%* |
|---|---|---|
| *MgK* | 66.1 | 89.2 |
| *GdL* | 17.8 | 03.7 |
| *YL* | 06.7 | 02.5 |
| *ZnK* | 08.7 | 04.4 |
| *ZrL* | 00.8 | 00.3 |

| *Element* | *Wt%* | *At%* |
|---|---|---|
| *MgK* | 87.5 | 97.3 |
| *GdL* | 08.8 | 01.5 |
| *YL* | 02.5 | 00.8 |
| *ZnK* | 00.8 | 00.3 |
| *ZrL* | 00.5 | 00.1 |

**Fig. 6.** (a) Transverse direction SEM image of the as-extruded specimen and the result of linear SEM-EDS; (b) Longitudinal direction SEM image of the as-extruded specimen; (c) EDS result of point A; (d) EDS result of point B.

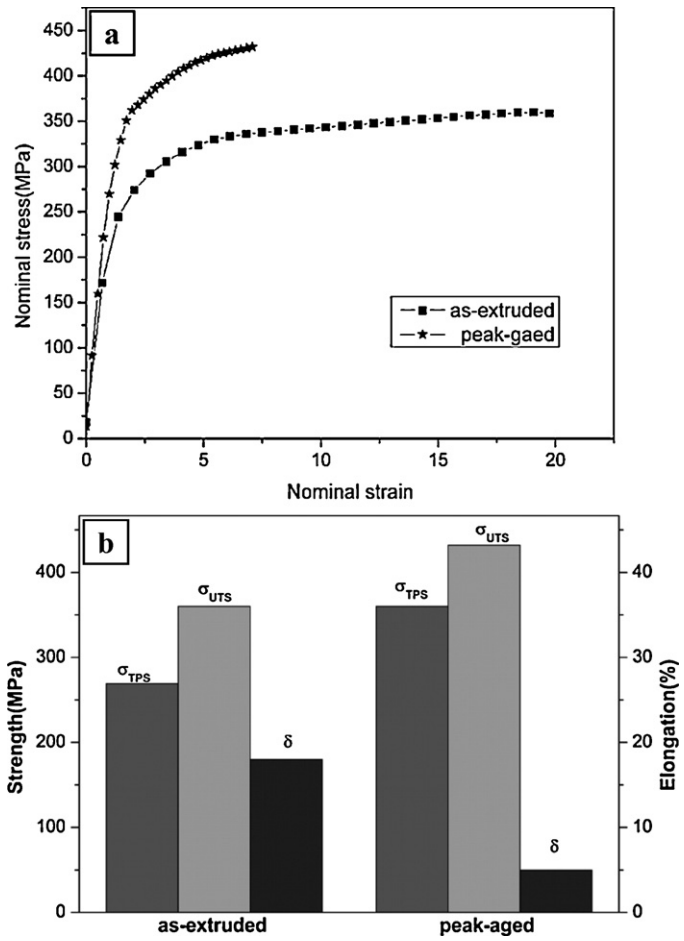


**Fig. 7.** (a) Nominal stress–strain curves of the as-extruded and peak-aged specimens; (b) Tensile properties of the as-extruded and peak-aged specimens.

ing models based on dislocation movement have been applied in as-extruded and peak-aged specimens.

### 4.1. Strengthening mechanism of as-extruded alloy

For as-extruded alloy, solute atoms and grain boundary should be considered as the main factors of preventing dislocation motion. When dislocations move in grain interior, solute atoms are the main obstacles. When dislocations move from one grain to another, grain boundaries should be the main barrier. Thus, the strengthening mechanism of as-extruded specimen should involve the following two contributions: solid solution strengthening and grain boundary strengthening.

#### 4.1.1. Solid solution strengthening

The contribution to the yield strength of solid solution atoms can be expressed by Eq. (1) [20]:

$$\sigma_y = \sigma_u + \frac{3.1\varepsilon G C^{1/2}}{700} \quad (1)$$

where $G$ is the shear modulus of the matrix ($1.66 \times 10^4$ MPa for Mg [21]). $\varepsilon$ is an experimental constant (0.74 for Mg–Gd series alloy [22]). $\sigma_u$ is the tensile yield strength (TYS) of pure Mg ($\sigma_u$ = 21 MPa [23]). $C$ is the concentration of the solutes in atomic percentage, and $C$ is up to the concentration of the solutes in supersaturated solid solution. The ratio of RE and Zn in Mg–10Gd–6Y–2Zn–0.6Zr alloy is 3.6:0.7 (at%), and it is much higher than that in LPSO structure. It is reasonable to assume all the Zn addition has been consumed by the LPSO structure, and then the surplus of RE addition is 2.55 at%, and this value is in agreement with the EDS result of the matrix (point B Fig. 6). So C can be determined as 2.55. Thus, the contribution of solid solution strengthening to TYS of the as-extruded specimen ($\sigma_{ey1}$) is 108 MPa.

#### 4.1.2. Grain boundary strengthening

The Hall–Petch Eq. (2) was employed to predict the contribution of grain boundary to yield strength of as-extruded specimens:

$$\sigma_y = \sigma_0 + Kd^{-1/2} \quad (2)$$

$\sigma_0$ is the intrinsic resistance of the lattice to dislocation motion (46.5 MPa for Mg–Gd alloys [24]), $K$ is the constant (164 MPa $\mu^{-1/2}$ for extruded-T5 Mg–Gd–Y alloys [25]), $d$ is the average grain size (4.7 μm for the as-extruded specimen). Therefore, the calculated contribution of grain boundary to the yield strength of the as-extruded is $\sigma_{ey2}$ = 122 MPa.

In summary, the calculated yield strength ($\sigma_{ey}$) is 230 MPa, and it is lower than that of the experimental value (269 MPa). The difference may be generated from the contribution of LPSO structures to yield strength, and there is no theoretical basis can be introduced to estimate the contribution of LPSO structures to yield strength. So it is not considered in the model.

### 4.2. Strengthening mechanism of peak-aged specimens

For the peak-aged specimens, the supersaturated solid solution decomposed. So the strengthening effect of the solutes translated into that of the $\beta'$ phase. Thus the precipitation and grain boundary should be considered as the main factors of preventing dislocation motion. Therefore, the strengthening mechanism of peak-aged specimen should involve the following two contributions: precipitation strengthening and grain boundary strengthening.

#### 4.2.1. Precipitation strengthening

The $\beta'$ plates form on the $\{1\bar{1}00\}_\alpha$ or $\{2\bar{1}\bar{1}0\}_\alpha$ prismatic planes of α-Mg, and the angle between the habit plane of the precipitate plates and $(0001)_\alpha$ slip plane is 90°. The cross-section of the prismatic plates intersected in the slip plane is rectangular in shape [26]. Nie [27] reported the effect of prismatic precipitate plates on dispersion strengthening in magnesium alloys based on Orowan strengthening mechanism. Therefore, the contribution of $\beta'$ phase to yield strength can be estimated by Eq. (3) [27]:

$$\sigma_y = \frac{Gb}{2\pi\sqrt{1-\nu}\left(0.825\sqrt{\frac{d_t t_t}{f}} - 0.393 d_t - 0.886 t_t\right)} \times \ln\frac{0.886\sqrt{d_t t_t}}{b} \quad (3)$$

where $b$ is the magnitude of the Burgers vector ($3.21 \times 10^{-10}$ m for Mg [28]), $\nu$ is the Poisson's ratio ($\nu$ = 0.35). $f$ is the volume fraction. $d_t$ and $t_t$ can be defined by the mean planar diameter $d_p$ ($=\pi d_t/4$) and the mean planar thickness $t_p$($=t_t$) [27]. For $\beta'$ phase, $f = 6 \times C\% = 15.3\%$, $d_p$ = 55.6 nm and $t_p$ = 8.3 nm, as shown in Fig. 8d, so $d_t$ = 70.8 nm and $t_t$ = 8.3 nm. Then the contribution of $\beta'$ phase to the yield strength ($\sigma_{ay1}$) is about 277 MPa.

#### 4.2.2. Grain boundary strengthening

The grain boundary strengthening of peak-aged specimen is identical to that of as-extruded specimen, so the contribution of the grain boundary to the yield strength of peak-aged specimen: $\sigma_{ay2}$ = 122 MPa.

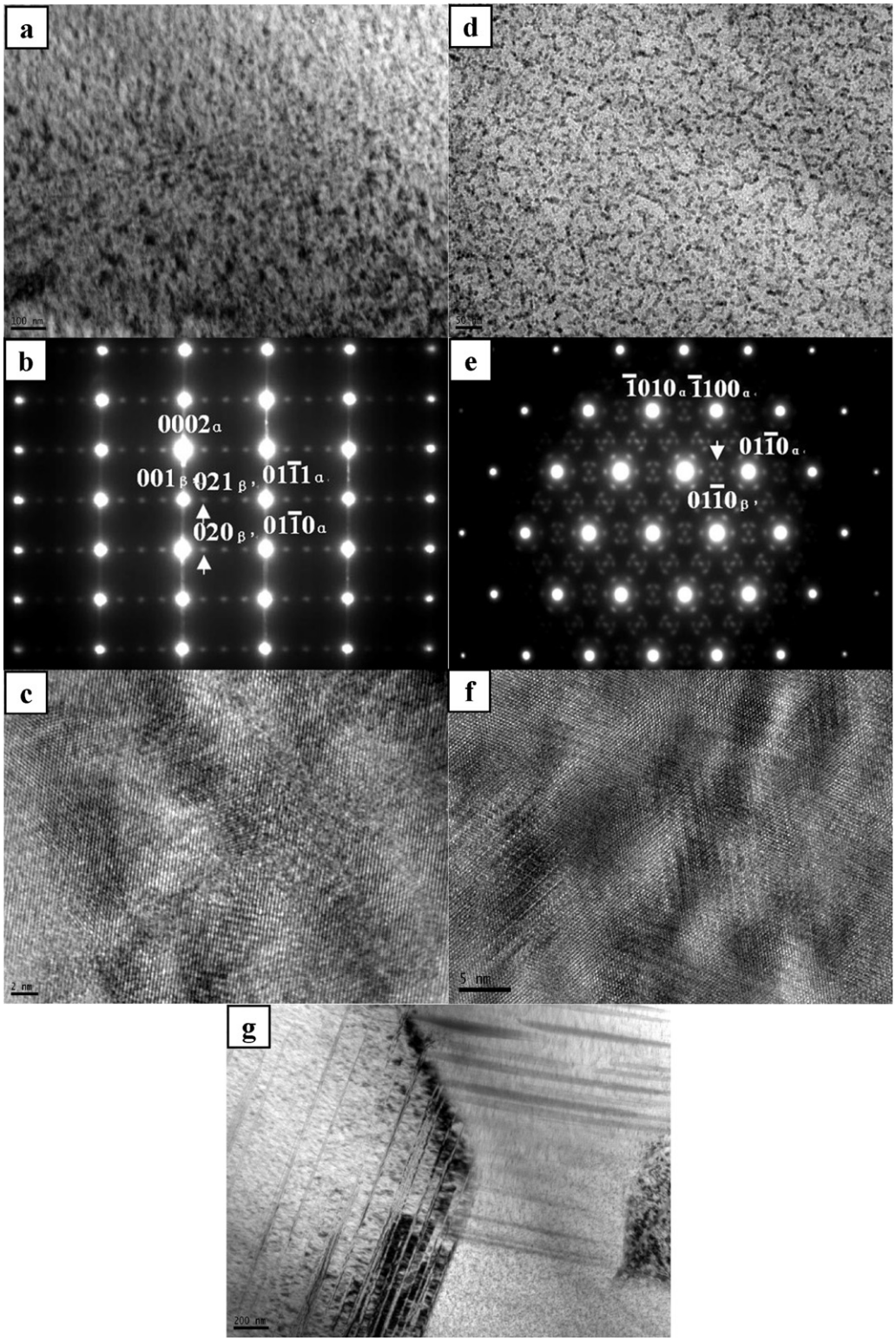


**Fig. 8.** (a) TEM BF image of the peak-aged specimen; (b) The corresponding SEAD pattern ($B//[2\ \bar{1}\ \bar{1}\ 0]$); (c) HRTEM image of the peak-aged specimen ($B//[2\ \bar{1}\ \bar{1}\ 0]$); (d) TEM BF image of the peak-aged specimen; (e) The corresponding SEAD pattern ($B//[0\,0\,0\,1]$); (f) HRTEM image of the peak-aged specimen ($B//[0\,0\,0\,1]$); (g) TEM BF image of the LPSO structure in different grains of the peak-aged specimen, accompanied with precipitation.

To sum up, the calculated yield strength of the peak-aged specimen ($\sigma_{ay}$) is 399 Mpa, a little higher than the experimental value (360 MPa as shown in Fig. 7b). The difference may be generated from the error of the parameters chosen in calculation and the defects from the preparation process of the specimens.

## 5. Conclusions

The microstructures and the tensile mechanical properties of Mg–10Gd–6Y–2Zn–0.6Zr alloy have been investigated. The effective strengthening models have been considered to pre-

dict the strength. The investigation can lead to the following conclusions:

LPSO structures with different forms are found in Mg–10Gd–6Y–2Zn–0.6Zr alloy: the block-shaped ones at grain boundaries and lamellar ones in the inner grains. 6H-type LPSO structures with ABCBCB′ stacking sequence are determined in the homogenized specimen, where A and B′ layers are significantly enriched by Gd, Y, and Zn.

The block-like LPSO structures have an inhibition effect on the growth of DRX grains during hot extrusion, and the lamellar LPSO structures can improve the distribution of the $\beta'$ phase.

The calculated yield strengths of the as-extruded and peak-aged specimens of alloy based on the prediction models suggest that the grain boundary is the main strengthening contributor of the as-extruded alloy. In addition, the sub-micron metastable phase of $\beta'$ is the main strengthening factor of the peak-aged alloy.

## Acknowledgments

This work was supported partly by the Natural Science Foundation of China (51074186) and the Open-End Fund for the Valuable and Precision Instruments of Central South University. The authors would like to thank Professor Ding Daoyun for providing writing assistance to the article, and the anonymous reviewers for supplying the helpful comments.

## References

[1] D. Wu, R.S. Chen, E.H. Han, J. Alloys Compd. 509 (2011) 2856–2863.
[2] L. Li, X.M. Zhang, C.P. Tang, Y.L. Deng, N. Zhou, Mater. Sci. Eng. A 527 (2010) 1266–1274.
[3] K. Liu, J. Meng, J. Alloys Compd. 509 (2011) 3299–3305.
[4] J.H. Zhang, Z. Leng, S.J. Liu, J.Q. Li, M.L. Zhang, R.Z. Wu, J. Alloys Compd. 509 (2011) 7717–7722.
[5] B.L. Xiao, Q. Yang, J. Yang, W.G. Wang, G.M. Xie, Z.Y. Ma, J. Alloys Compd. 509 (2011) 2879–2884.
[6] T. Peng, Q.D. Wang, J.B. Lin, M.P. Liu, H.J. Roven, Mater. Sci. Eng. A 528 (2011) 1143–1148.
[7] X.M. Zhang, C.P. Tang, Y.L. Deng, L. Yang, W.J. Liu, J. Alloys Compd. 509 (2011) 6170–6174.
[8] W.C. Liu, J. Dong, X. Song, J.P. Belnoue, F. Hofmann, W.J. Ding, A.M. Korsunsky, Mater. Sci. Eng. A 528 (2011) 2250–2258.
[9] G. Sha, J.H. Li, W. Xu, K. Xia, W.Q. Jie, S.P. Ringer, Mater. Sci. Eng. A 527 (2010) 5092–5099.
[10] G. Barucca, R. Ferragut, F. Fiori, D. Lussana, P. Mengucci, F. Moia, G. Riontino, Acta Mater. 59 (2011) 4151–4158.
[11] K. Liu, J.H. Zhang, G.H. Su, D.X. Tang, L.L. Rokhlind, F.M. Elkind, J. Meng, J. Alloys Compd. 481 (2009) 811–818.
[12] M. Yamasaki, M. Sasaki, M. Nishijima, K. Hiraga, Y. Kawamura, Acta Mater. 55 (2007) 6798–6805.
[13] S. Zhang, G.Y. Yuan, C. Lu, W.J. Ding, J. Alloys Compd. 509 (2011) 3515–3521.
[14] T. Itoi, T. Seimiya, Y. Kawamura, M. Hirohashi, Scripta Mater. 51 (2004) 107–111.
[15] D.J. Li, X.Q. Zeng, J. Dong, C.Q. Zhai, Trans. Nonferrous Met. Soc. China 18 (2008) s117–s121.
[16] Y. Gao, Q.D. Wang, J.H. Gu, Y. Zhao, Y. Tong, D.D. Yin, J. Alloys Compd. 477 (2009) 374–378.
[17] K. Liu, L.L. Rokhlin, F.M. Elkin, D.X. Tang, J. Meng, Mater. Sci. Eng. A 527 (2010) 828–834.
[18] E. Abe, Y. Kawamura, K. Hayashi, A. Inoue, Acta Mater. 50 (2002) 3845–3857.
[19] T. Honma, T. Ohkubo, S. Kamado, K. Hono, Acta Mater. 55 (2007) 4137–4150.
[20] R.W. Hertzberg, Deformation and Fracture Mechanics of Engineering Materials, third ed., Wiley PUB, 1989.
[21] M. Mabuchi, K. Higashi, Acta Mater. 44 (1996) 4611–4618.
[22] Z. Yang, J.P. Li, Y.C. Guo, T. Liu, F. Xia, Z.W. Zeng, M.X. Liang, Mater. Sci. Eng. A 454–455 (2007) 274–280.
[23] L.L. Rokhlin, Magnesium Alloys Containing Rare Earth Metals, Taylor and Francis, 2003, p. 83.
[24] L. Gao, R.S. Chen, E.H. Han, J. Alloys Compd. 481 (2009) 379–384.
[25] S.M. He, X.Q. Zeng, L.M. Peng, X. Gao, J.F. Nie, W.J. Ding, J. Alloys Compd. 427 (2007) 316–323.
[26] L. Gao, R.S. Chen, E.H. Han, J. Mater. Sci. 44 (2009) 4443–4454.
[27] J.F. Nie, Scripta Mater. 48 (2003) 1009–1015.
[28] H.J. Frost, M.F. Ashbv, Deformation-Mechanism Maps, Pergamon Press, Oxford, 1982, p. 44.